Higher-dimensional quasicrystalline approach to the Hofstadter butterfly topological-phase band conductances: Symbolic sequences and self-similar rules at all magnetic fluxes

Gerardo Naumis

Departamento de Sistemas Complejos, Instituto de Física, Universidad Nacional Autónoma de México (UNAM), Apartado Postal 20-364, 01000 México, Distrito Federal, México

(Received 28 May 2019; revised manuscript received 5 August 2019; published 1 October 2019)

The topological properties of the quantum Hall effect in a crystalline lattice, described by Chern numbers of the Hofstadter butterfly quantum phase diagram, are deduced by using a geometrical method to generate the structure of quasicrystals: the cut and projection method. Based on this, we provide a geometric unified approach to the Hofstadter topological-phase diagram at all fluxes. Then we show that for any flux, bands conductances follow a two-letter symbolic sequence. As a result, conductances at different fluxes obey inflation/deflation rules as the ones observed to build quasicrystals. The symbolic sequences are given by the Sturmian coding of the flux and can be found by considering a circle map, a billiard, or trajectories on a torus. Simple and fast techniques are thus provided to obtain Chern numbers at all magnetic fluxes. This approach allows one to understand the global fractality of the butterfly in terms of Farey sequences and trees.

DOI: 10.1103/PhysRevB.100.165101

I. INTRODUCTION

Historically, the quantum Hall effect (QHE) was the first discovered manifestation of a topological phase [1] although the electronic spectrum in a square lattice as a function of the magnetic flux was first found by Hofstadter [2]. As seen in Fig. 1, this spectrum is a beautiful fractal called the Hofstadter butterfly. It has been measured using different kinds of effective systems, but only recently it has been possible to measure it in atomic systems [3]. In this moment, there is a huge interest in this problem, as there is a connection yet to understand between the solutions of the QHE and the superconductivity observed in graphene over graphene rotated at magic angles [4].

Also, the interest in the Hofstadter butterfly has been growing in the context of topological insulators and two-dimensional materials [5–10]. These insulators are exotic states of matter which are insulators in the bulk but conduct along the edges [1,5,11]. In the QHE, such states are characterized by topologically protected gapless boundary modes, known as *edge-Chern* modes. These modes manifest the nontrivial band structure topology of the bulk [1] and their number equals the topological integer known as the Chern number (σ_r). These Chern numbers are the quanta of the Hall conductance for a system under a constant magnetic field [1]. Each Chern quantum number is thus associated with a gap r. The Chern number for each gap is obtained by solving a Diophantine equation [11]. Recently, there have been many works devoted to find the Hofstadter butterfly phases for other systems [12,13], usually related to work on graphene [9,14].

There is a vast amount of literature dedicated to the subject (the original paper by Hofstadter has more than 4000 citations); most of it usually looks for scaling properties for a given flux or looks at replicas of the Landau states and not the whole fractal, although now there is a growing interest in the global fractality and its relationship to other fractals [15,16]. In particular, there are many numerically observed relationships in the global fractality of the topological-phase diagram of the butterfly not yet explained theoretically [15,16]. Moreover, the Hofstadter butterfly, obtained form the Harper equation [17–19] (which is also known as the almost Mathieu operator problem in mathematics), is considered as one of the first examples of a quasiperiodic Hamiltonian, yet many works treat the QHE with different methodologies than the ones used to describe quasicrystals [20,21]. In a previous paper, it was shown that the Harper potential and the Fibonacci chain were just examples of different kinds of trigonometric potentials [22]. Then one can follow the transformation of the Harper model into the Fibonacci one just by adding harmonics to the potential, leading to a "Fibonacci butterfly" made from a square well potential [22].

Later on, Kraus and Zilberberg suggested that the Harper model and the Fibonacci chain were within the same topological class [23,24]. Key to the topological characterization of QCs is a parameter that shifts the starting point of the sequences [23,24]. However, if we take the common definition that one can deform one model to the other without closing any gap, this does not hold for the two models [25]. If, one takes the weaker notion so that for all irrational frequencies one can deform one model to the other without closing any gap, then the claim may be right, although it is not known if indeed this is the case. Also, a novel manifestation of the topology that is unique to QCs has been found, since *band edges modes* encode topological invariants in their spatial profiles leading to a "Chern beating" phenomena, as Chern doublets are convoluted with a fractal ground state [26]. Anyway, nowadays there are acoustic [27] and metamaterial equivalent systems [28] to test all these ideas that connect quasicrystals with topological modes.

Thus, this article proposes to use a common, unified quasicrystal-based language to solve the following problem:

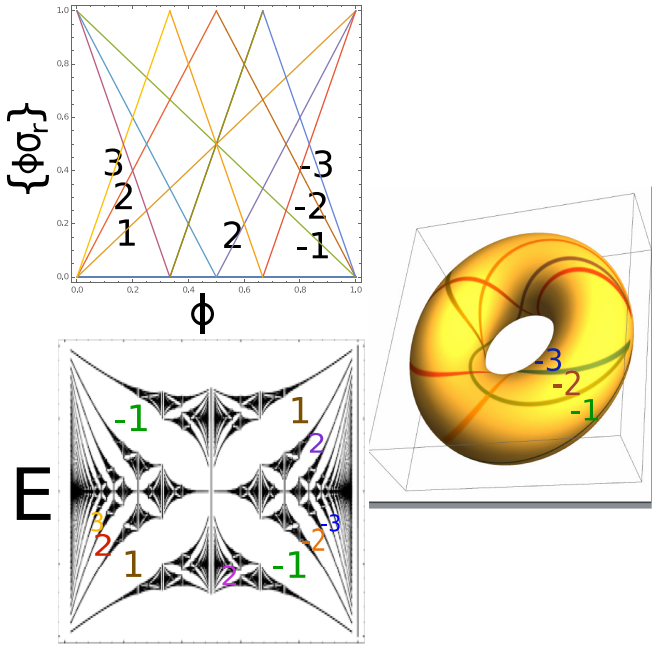

FIG. 1. (Top left) Topological map of the Hofstadter butterfly for the first Chern numbers, i.e., the filling fractions $r/q = \{\phi\sigma_r\}$ for $\sigma_r = \pm 1, \pm 2, \pm 3$ as a function of ϕ. (Bottom left) The map is compared with the Hofstadter butterfly where each gap has a Chern number associated with its conductance. Each gap associates with a line in the map. To the right, the topological map of the Hofstadter butterfly on a torus. This map is obtained by defining two angles $\Phi = 2\pi\phi$ and $\theta = 2\pi\{\sigma_r\phi\}$. Here Φ is the azimuth angle, also known as the "toroidal" direction, and θ is the "poloidal" angle. For each Chern number σ_r, a trajectory on the torus is obtained, represented here with a different color and with its corresponding label. Note how trajectory crossings produce topological sequences near Van Hove singularities [29].

the actual dissociation between topological phases and quasicrystals [30]. Moreover, this allows one to explain relationships between phases at different fluxes which at this moment were only known numerically. First we formalize the relationship between the topological properties of the Hofstadter butterfly using a classic cut and projection quasicrystallographic description [19,31–33] by writing in this language a solution previously found in another paper [29]. It is worthwhile mentioning that these ideas have already been used for other systems [9,13,14,34] such as, for example, density wave states in the presence of an external magnetic field[35]. The second purpose is to relate symbolic sequences to the conductance and then explain the relationship between electron diffraction and topological phases.

The layout of this work is the following. In Sec. II we revise a method developed previously by the author to find the Chern numbers. In Sec. III the method is written in terms of the cut and projection method, while Sec. IV is devoted to find the conductance as symbolic sequences. As shown in Sec. V, this allows one to obtain simple methods to find Chern numbers. In Sec. VI we relate the cut and projection method with the Harper potential properties, and finally, the conclusions are given.

II. TOPOLOGICAL-PHASE DIAGRAM: HIGHER-DIMENSIONAL APPROACH

In this section, we will consider some general properties of the Hofstadter butterfly topological map. As shown by the author in a previous paper, this topological-phase diagram can be obtained from a higher-dimensional approach [29]. Here we outline the main results to introduce the connection with the cut and projection method. First we observe that the Hofstadter spectrum (see Fig. 1) is produced by considering a square lattice in a uniform magnetic field. For a magnetic flux $\phi = p/q$, where p and q are integers, this results in the Harper equation [18],

$$\psi^r_{m+1} + \psi^r_{m-1} + V(m)\psi^r_m = E_r\psi^r_m, \tag{1}$$

where ψ^r_m are the electron wave functions at site m for the band r with energies E_r. The Harper potential is [18]

$$V(m) = 2\lambda\cos(2\pi m\phi + 2\pi\nu_y), \tag{2}$$

and $0 \leqslant \nu_y \leqslant 1/2$ for p odd and $0 \leqslant \nu_y \leqslant q/2p$ for p even [5].

The energy E as a function of the flux ϕ produces the Hofstadter butterfly shown in Fig. 1. For a given flux ϕ, a Chern number σ_r is associated with the gap r, counted from the bottom to the top of the spectrum. The Chern number gives the conductance of such a gap [1]. The gap and its corresponding Chern number is obtained by solving the following Diophantine equation [1,11,36],

$$r = p\sigma_r + q\tau_r, \tag{3}$$

where τ_r is an integer. To solve this equation we use a higher dimension approach as follows [29]. As seen in Fig. 2, define a flux vector,

$$\boldsymbol{F}(\phi) = (p, q), \tag{4}$$

and a topology vector,

$$\boldsymbol{T}_r = (\sigma_r, \tau_r). \tag{5}$$

In this language, the Diophantine is written as

$$r = \boldsymbol{F}(\phi)\cdot\boldsymbol{T}_r. \tag{6}$$

Thus the gap index r is the projection of the topology vector onto the flux vector. This is no other than the distance between the point (σ_r, τ_r) and a line perpendicular to $\boldsymbol{F}(\phi)$.

This suggests a method to solve the Diophantine equation. First we take a two-dimensional (2D) space, in which any point is denoted as $\boldsymbol{X}$. As seen in Fig. 2, we consider a vectorial subspace of lower dimensionality $E^{||}$, in this case a line perpendicular to $\mathbf{F}(\phi)$. Points in this line have the form $\boldsymbol{X}\cdot\boldsymbol{F}(\phi) = 0$.

A perpendicular subspace $E^{\perp}$ is now defined, as indicated in Fig. 2. All possible solutions to the Diophantine are contained in the family of parallel lines $\boldsymbol{X}\cdot\boldsymbol{F}(\phi) = r$. This is equivalent to find all integer coordinates that are within the parallel lines $\boldsymbol{X}\cdot\boldsymbol{F}(\phi) = 0$ and $\boldsymbol{X}\cdot\boldsymbol{F}(\phi) = q$. We will call this region the "band."

To find the solution of the Diophantine equation we proceed as follows.

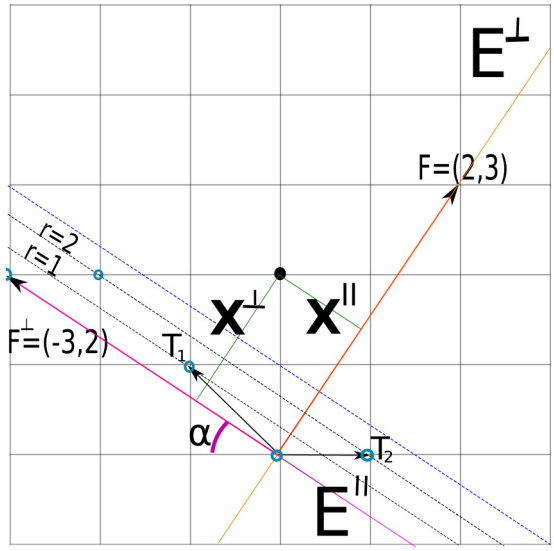

FIG. 2. Cut and projection method applied to find the solutions of the Diophantine equation given by Eq. (3). Here, the flux vector is chosen to give $\phi = \tan\alpha = 2/3$. The set of parallel lines gives possible solutions for $\boldsymbol{F}(\phi)\cdot\boldsymbol{T}_r = r$ for each gap r. For example, $\mathbf{T}_1$ and $\mathbf{T}_2$ are solutions for $r = 1$ and $r = 2$; others are indicated by open circles. Notice the periodicity of the solutions. In general, the flux vector F defines a parallel subspace $E^{||}$, while $E^{\perp}$ is a perpendicular subspace defined by $F^{\perp}$. Any point $\boldsymbol{X}$, indicated by a black dot, can be decomposed as $\boldsymbol{X} = \boldsymbol{X}^{||} + \boldsymbol{X}^{\perp}$. Valid solutions require $\boldsymbol{X}$ to have integer coordinates and $|\boldsymbol{X}^{\perp}| < 1/\sqrt{1+\phi^2}$. Physically, $\boldsymbol{X}^{\perp}$ is the band filling ratio r/q.

(1) Consider a 2D square lattice, such that $\boldsymbol{X} = (n_1, n_2)$ with n_1, n_2 any integer.

(2) Choose points such that $\boldsymbol{X}\cdot\boldsymbol{F}(\phi) \leqslant q$.

(3) Then identify $n_1 = \sigma_r$ and $n_2 = \tau_r$. It is easy to show that integer coordinates points $\boldsymbol{X}$ within the band satisfy [29]

$$\tau_r = -\lfloor \phi\sigma_r \rfloor, \tag{7}$$

where $\lfloor z \rfloor$ denotes the floor function of z. The floor function allows one to select points $\boldsymbol{X}$ that fall inside the band. Thus gaps are labeled by the coordinates of a two-dimensional lattice,

$$(\sigma_r, \tau_r) = (\sigma_r, -\lfloor \phi\sigma_r \rfloor). \tag{8}$$

By using that any number z can be written as $z = \lfloor z \rfloor + \{z\}$, where $\{z\}$ denotes the fractional part of z (observe that a negative number $-x$, we have $\{-x\} = 1 - \{x\}$), we can express τ_r as

$$r = q\{\phi\sigma_r\}. \tag{9}$$

Equation (9) can be inverted using the same methodology giving the Chern numbers as a function of the gap index,

$$\sigma_r = \left(\frac{q}{2} - q\left\{\phi r + \frac{1}{2}\right\}\right)\zeta, \tag{10}$$

where the variable $\zeta = (-1)^{q-p}$ determines the sign. We will refer to these two previous equations as the hull functions. Several properties are deduced from Eq. (9) and Eq. (10). For rational ϕ, we have the following.

(1) The solutions are periodic up to a vector $(-q, p)$, i.e., Chern numbers have a period q while τ_r has period p.

(2) The solutions for conductance correspond to Cherns between $-q/2$ and $q/2$. This defines a "first Brillouin zone" for Cherns.

(3) The solution $\boldsymbol{T}_1$ for $r = 1$ always exists, since a Diophantine equation of the form $ax + by = 1$ always has a solution if p and q are relative primes.

(4) All solutions are obtained from the $r = 1$ solution, which we call the fundamental one. To show this, consider the solution for $r = 1$. It satisfies

$$\boldsymbol{F}(\phi)\cdot\boldsymbol{T}_1 = 1, \tag{11}$$

and multiplying this equation by r, it will satisfy the Diophantine equation Eq. (6). Then,

$$\boldsymbol{T}_r = r\boldsymbol{T}_1. \tag{12}$$

(5) Combining the previous properties, the solutions are given by

$$\boldsymbol{T}_r = r\boldsymbol{T}_1 + s\boldsymbol{F}^{\perp}, \tag{13}$$

where s is chosen to have Cherns between $-q/2$ and $q/2$. This is equivalent to take solutions modulus q in σ_r and modulus p in τ_r.

If we think of Eq. (9) as a function of ϕ for each integer σ_r, we obtain the Claro-Wannier map [37] seen in Fig. 1(a), which can be compared with the original butterfly in Fig. 1(b). Each line corresponds to a gap and the slope of the line gives the Chern number. Figure 1(b) shows the Chern labeling on the butterfly [29]. The saw tooth function $\{\sigma_r\phi\}$ has period $1/\sigma_r$, and thus can be used to wrap a torus for each Chern number σ_r. So consider the map $\Phi = 2\pi\phi$ and $\theta = 2\pi\sigma_r\phi$ as a parametrization of the torus, in which Φ is the azimuth angle, known as the "toroidal" direction, and θ is the "poloidal" angle. In Fig. 1(c) we present the trajectories on the torus for the first Chern numbers. Notice how Fig. 1(c) is obtained by projecting the Claro-Wannier diagram of Fig. 1 onto a torus. It is interesting to observe that trajectory crossings corresponding to Van Hove singularities existing at all band centers due to saddle points of the energy dispersion [29].

III. CUT AND PROJECTION: STRUCTURE OF QUASICRYSTALS AND TOPOLOGICAL PHASES

The method exposed in the previous section turns out to be a very special case of the cut and project method, used to generate the structure of quasicrystals [21,33]. For further reference, let us now revisit this method. To build the structure of a quasicrystal, consider points $\boldsymbol{X}$ in a D-dimensional space periodic lattice,

$$\boldsymbol{X} = \sum_{j=1}^{D} n_j\hat{\boldsymbol{e}}_j, \tag{14}$$

where $\hat{\boldsymbol{e}}_j$ are the lattice vectors of a hypercubic ($D > 3$), cubic ($D = 3$) or square lattice ($D = 2$). These lattice points are projected onto a subspace $E^{||}$ using a projection operator $\hat{\Pi}(\boldsymbol{X})$. This projection will be called $\boldsymbol{X}^{||}$. A perpendicular subspace $E^{\perp}$ to $E^{||}$ is now defined. Any point $\boldsymbol{X}$ is decomposed as

$\boldsymbol{X} = \boldsymbol{X}^{||} + \boldsymbol{X}^{\perp}$, where $\boldsymbol{X}^{\perp}$ is the projection onto $E^{\perp}$. Not all points $\boldsymbol{X}$ are selected to build the quasicrystal. Instead, points $\boldsymbol{X}$ are selected by using a band function $W(\boldsymbol{X}^{\perp})$ such that an acceptance width is given in the $E^{||}$ space, resulting in

$$\boldsymbol{R} = \hat{\Pi}(\boldsymbol{X}) W(\boldsymbol{X}^{\perp}) = \boldsymbol{X}^{||} W(\boldsymbol{X}^{\perp}), \tag{15}$$

where usually the band width, although it can be any constant, is taken as one,

$$W(\boldsymbol{X}^{\perp}) = \begin{cases} 1 \text{ if } |\boldsymbol{X}^{\perp}| < 1 \\ 0 \text{ if } |\boldsymbol{X}^{\perp}| \geqslant 1 \end{cases}. \tag{16}$$

Since the points $\boldsymbol{X}$ form a lattice in D dimensions, using the linearity of the operator, it is easy to prove that points in the quasicrystal are given by

$$\boldsymbol{R} = \left(\sum_{j=1}^{D} n_j \boldsymbol{q}_j \right) W(n_1, n_2, ..., n_D), \tag{17}$$

where n_j are integers and $\boldsymbol{q}_j$ is the projection of the higher-dimensionality base into $E^{||}$, i.e., $\boldsymbol{q}_j = \hat{\Pi}(\hat{\boldsymbol{e}}_j)$.

Let us now use this method to build one-dimensional quasicrystals and rational approximants. As explained in Fig. 2, we first consider a square lattice. The subspace $E^{||}$ is now a line inclined with angle $-\alpha$, while $E^{\perp}$ is a line perpendicular to it.

The points $\boldsymbol{X}$ in two dimensions with integer coordinates have the form $\boldsymbol{X} \equiv \boldsymbol{X}_{n_1,n_2} = (n_1, n_2)$. The projection in $E^{||}$ is given by

$$\boldsymbol{X}^{||} \equiv \boldsymbol{X}^{||}_{n_1,n_2} = n_1 q_1 - n_2 q_2, \tag{18}$$

where

$$q_1 = \cos\alpha = \frac{q}{\sqrt{p^2+q^2}};\ q_2 = \sin\alpha = \frac{p}{\sqrt{p^2+q^2}}, \tag{19}$$

and the perpendicular projection is

$$\boldsymbol{X}^{\perp} \equiv \boldsymbol{X}^{\perp}_{n_1,n_2} = n_1 q_2 + n_2 q_1. \tag{20}$$

From this, the band condition (16) results here in a relationship between n_1 and n_2, to give $W(\boldsymbol{X}^{\perp}) = \delta_{n_1,-\lfloor n_1 \tan\alpha \rfloor}$, where δ_{ij} is the Kronecker delta of i and j. Finally, using the projection of the basis vectors $\hat{\boldsymbol{e}}_1 = (1, 0)$ and $\hat{\boldsymbol{e}}_2 = (0, 1)$ into the line $E^{||}$, we obtain the positions along the sequence,

$$R_{n_1} \equiv \boldsymbol{X}^{||}_{n_1,n_2} W\left(\boldsymbol{X}^{\perp}_{n_1,n_2}\right) = n_1 q_1 + \lfloor n_1 \tan\alpha \rfloor q_2. \tag{21}$$

For irrational $\tan\alpha$, the sequence is quasiperiodic. The famous Fibonacci chain is obtained by using $\tan\alpha = \tau^{-1}$, where $\tau^{-1} = (\sqrt{5}-1)/2$ is the inverse golden mean. This method can be adapted to generate quasicrystals in two and three dimensions by using appropriate analytical expressions for the window function [38,39].

It is worthwhile mentioning that R can be written as an average periodic chain, plus a fluctuation part. Using the identity $x = \lfloor x \rfloor + \{x\}$,

$$R_{n_1} = n_1 \langle q \rangle - \{n_1 \tan\alpha\} q_2, \tag{22}$$

where $\langle q \rangle = q_1 + \tan\alpha q_2$ is an average lattice parameter and the fractional part is the fluctuation part. The distances between consecutive points is given by

$$\left|\delta R_{n_1}\right| = [\{(n_1+1)\tan\alpha\} - \{n_1 \tan\alpha\}] q_2. \tag{23}$$

Notice that other approximants or quasicrystals in the same local isomorphism class can be obtained by performing a translation of the width function along $E^{\perp}$. These extra degrees of freedom are known as phasons, which are related to the extra phases that appear in the Fourier transform when compared with a normal crystal. If the shift along $E^{\perp}$ is κ, then the sequence is transformed into

$$R_{n_1} = n_1 q_1 + \lfloor n_1 \tan\alpha + \kappa \rfloor q_2, \tag{24}$$

or written as an average plus a fluctuation,

$$R_{n_1} = \kappa q_2 + n_1 \langle g \rangle - \{n_1 \tan\alpha + \kappa\} q_2, \tag{25}$$

which shows that κ shifts the sequence.

Now we can see how the topological phases of the Hofstadter butterfly are determined by the same method used to build the quasicrystal. We set $\tan\alpha = \phi$ and consider a higher-dimensional point $\boldsymbol{X} = \boldsymbol{X}_{\sigma_r,\tau_r} = (\sigma_r, \tau_r)$ representing a possible topological phase. The distance between this topological-phase point and the line $E^{||}$ is given by

$$\left|\boldsymbol{X}^{\perp}_{\sigma_r,\tau_r}\right| = \frac{\boldsymbol{X}_{\sigma_r,\tau_r} \cdot \boldsymbol{F}(\phi)}{|\boldsymbol{F}(\phi)|}, \tag{26}$$

and by using Eqs. (8) and (9), we obtain

$$\left|\boldsymbol{X}^{\perp}_{\sigma_r,\tau_r}\right| = \frac{r}{\sqrt{p^2+q^2}} = \frac{q}{\sqrt{p^2+q^2}} \{\sigma_r \phi\}. \tag{27}$$

Thus $|\boldsymbol{X}^{\perp}_{\sigma_r,\tau_r}|$ determines the filling fraction r/q, and the band has width $1/\sqrt{1+\phi^2}$. From the previous equation, it is clear there is a deep connection between the methods to build quasicrystals and topological phases. We will explore such connections in the forthcoming sections,

IV. BAND CONDUCTANCES AS SYMBOLIC SEQUENCES

Let us first explain how the conductance is related to symbolic sequences akin to the structure of quasicrystals and its rational approximants. In general, the contribution of a band r to the conductance is given by the difference between the Chern numbers associated with each band edge [11],

$$\sigma_B(r) = (\sigma_{r+1} - \sigma_r), \tag{28}$$

where here the band and gap conductance is measured in units of $\frac{e}{h}$. By using Eq. (10) in the previous definition, we obtain

$$\sigma_B(r) = \zeta q\left(\left\{\phi r + \tfrac{1}{2}\right\} - \left\{\phi(r+1) + \tfrac{1}{2}\right\}\right). \tag{29}$$

This is precisely the distance between consecutive points in a sequence obtained from the cut and projection methods as in Eq. (25), i.e., the set of distances between points in a rational approximant or in a quasicrystal [33,40]. To see this, observe that the function $\{x\}$ has the property $\{a+b\} = \{a\} + \{b\}$ if $\{a\} + \{b\} < 1$ and $\{a+b\} = (\{a\} + \{b\}) - 1$ if $\{a\} + \{b\} > 1$. Thus, it turns out that $\sigma_B(r)$ only takes two values, $-\zeta p$ and $\zeta(q-p)$. We map these two values to the letters L and S. For $\zeta = 1$, i.e., $q-p$ even,

$$-p \to S, \tag{30}$$

$$(q-p) \to L, \tag{31}$$

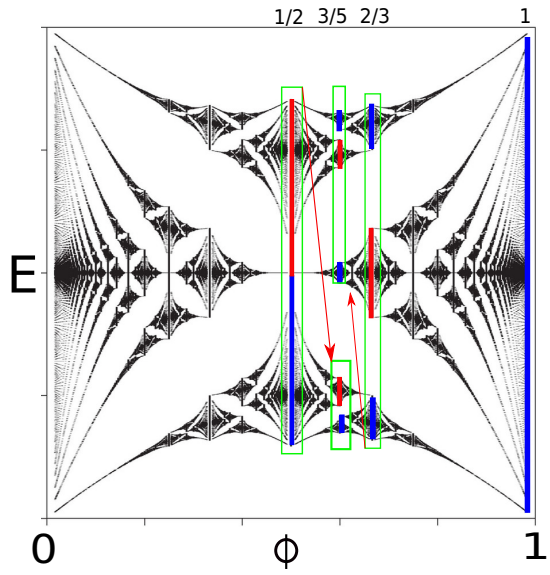

FIG. 3. Some symbolic sequences for band conductance given in Table I, overimposed on the Hofstadter butterfly. Bands with index L are indicated in blue, while bands with S are in red. The sequence for $\phi = 3/5$ is obtained by joining the sequences $\phi = 1/2$ and $\phi = 2/3$, as indicated at the top of the figure and by the green boxes. Notice the inflation/deflation rules and the scaling of bands.

while for $\zeta = -1$, i.e., $q - p$ odd,

$$p \to S, \tag{32}$$

$$(p - q) \to L. \tag{33}$$

In Fig. 3 we show some sequences on the original Hofstadter butterfly. For each rational ϕ, the periodicity of the sequence is given by q. In fact, by comparing Eqs. (28) and (23) and setting $\kappa = 1/2$, we just proved that the band conductance is proportional to the fluctuation part of the sequence,

$$\sigma_B(r) = \delta R_{r+1}. \tag{34}$$

To further understand the previous results, let us denote the band conductance sequences for a given ϕ as $S_B(\phi)$. In Table I we show for several fluxes the gap index r and its associated Chern number σ_r, as well as the band conductance corresponding symbol. In these examples, each flux was chosen to match the first rational approximant of the inverse golden mean $(\sqrt{5} - 1)/2$, given by the ratio of two successive Fibonacci numbers $\phi_j = F(j-1)/F(j)$. The j-esim Fibonacci number is given by $F(j) = F(j-2) + F(j-1)$, with $F(0) = 1$ and $F(1) = 1$.

As predicted by Eq. (29), a symbolic sequence is obtained for the band conductances. Moreover, we observe that in fact, the sequences for different fluxes also follow a recursive relation similar to that used for Fibonacci chains, i.e., from

TABLE I. Gap number r, the associated Chern number σ_r, the band conductance given by $\sigma_B(r) = \sigma_{r+1} - \sigma_r$, and the associated symbolic sequence $S(\phi)$ for fluxes chosen as the first golden mean approximants. Notice how a given symbolic sequence is given by joining the previous two sequences. Such construction is seen in Fig. 3, where band conductances follow the same pattern. Also observe that sequences are similar to the usual Fibonacci ones up to a global phason due to the factor 1/2 that appears in Eq. (29). Here all sequences are the same as in Fibonacci except for $\phi = 3/5$.

	$\phi = 1$ ($\zeta = 1$)								
r	0	1							
σ_r	0	1							
$\sigma_B(r)$	1	–							
$S(1)$	L	–							
	$\phi = 1/2$ ($\zeta = -1$)								
r	0	1	2						
σ_r	0	−1	0						
$\sigma_B(r)$	−1	1	–						
$S(1/2)$	L	S	–						
	$\phi = 2/3$ ($\zeta = -1$)								
r	0	1	2	3					
σ_r	0	−1	1	0					
$\sigma_B(r)$	−1	2	−1	–					
$S(2/3)$	L	S	L	–					
	$\phi = 3/5$ ($\zeta = 1$)								
r	0	1	2	3	4	5			
σ_r	0	2	−1	1	−2	0			
$\sigma_B(r)$	2	−3	2	−3	2	–			
$S(3/5)$	L	S	L	S	L	–			
	$\phi = 5/8$ ($\zeta = -1$)								
r	0	1	2	3	4	5	6	7	8
σ_r	0	−3	2	−1	−4	1	−2	3	0
$\sigma_B(r)$	−3	5	−3	−3	5	−3	5	−3	–
$S(5/8)$	L	S	L	L	S	L	S	L	–

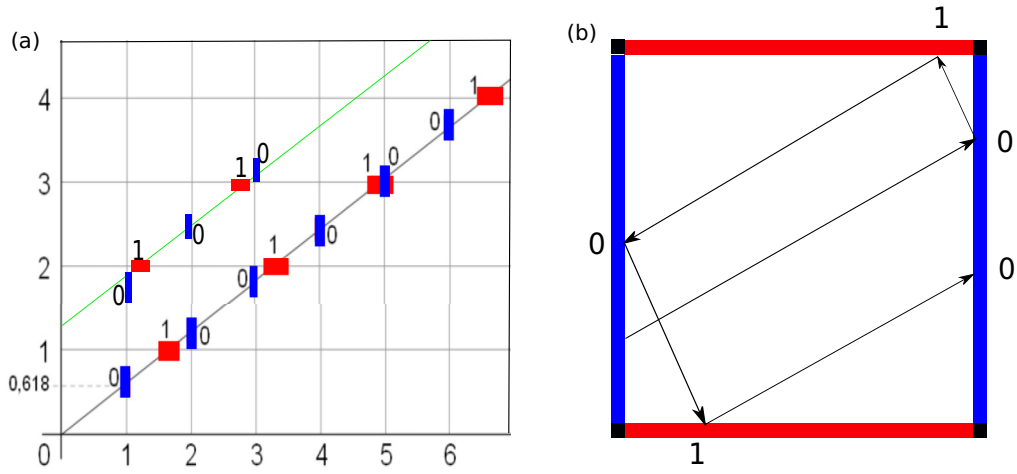

FIG. 4. (a) Sturmian coding of $\phi = 3/5$. The black line going through the origin is the usual Sturmian coding for a flux $\phi = 3/5 = 0.618$. This is an approximant of the golden mean. The slope of the inclined line is ϕ. Each intersection is labeled 0 or 1 depending on the kind of intersection with the grid. The displaced green line is the same sequence with a global phason shift, and can be compared with the sequence of Table I. Observe how the color coding is the same as in the Hofstadter butterfly conductances seen at $\phi = 3/5$ in Fig. 3. (b) The coding can be found in a square colored billiard, in which each kind of reflection with a vertical or horizontal wall is coded with a 0 or 1. The reason is that one can fold the trajectory shown in (a) by thinking of each intersection with the grid as a mirror.

Table I we see that

$$S(\phi_j) = S(\phi_{j-2}) \oplus S(\phi_{j-1}), \tag{35}$$

where the sign $\oplus$ means join two sequences. For example, $S(5/8) = S(2/3) \oplus S(3/5)$.

Although superficially this sequence looks like the usual Fibonacci sequence; in fact it is very important to remark that the order of chain joining $S(\phi_{j-2}) \oplus S(\phi_{j-1})$ is reversed when compared to the Fibonacci chain in which $S(\phi_{j-1}) \oplus S(\phi_{j-2})$. For example, in Table I we see that the sequence for $\phi = 3/5$ is *LSLSL* while the Fibonacci is *LSLLS*. The reader may wonder why they are different or "reversed." The answer lies in the factor $1/2$ in Eq. (28). This is equivalent to a global phason that shifts the sequence. Then one needs to compare shifts of a sequence in order to decide if they are or are not in the same isomorphism class [41]. For example, we can apply several phason shifts to the sequence *LSLSL*. This is equivalent to an origin shift with cyclic boundary conditions. We obtain the following sequences $LSLSL \to LLSLS \to SLLSL \to LSLLS$. The last sequence is the usual Fibonacci sequence and thus both sequences are in the same isomorphism class.

As is well known, an alternative way to generate such sequences is by using deflation, inflation, or recursive rules [21,31]. The important result here is that we can relate different fluxes by such deflation/inflation rules. In Fig. 3 we explain the previous constructions on the original Hofstadter butterfly. Figure 3 is meant to be compared with the sequence of Table I.

Clearly, for other rational sequences such as for the silver, bronze, etc., means one can build such rules, and in fact, the general inflation/deflation rules generated by Eq. (29) have been extensively studied in the context of quasicrystals [21,31].

A neat and suggestive way to write the symbolic sequences associated with each ϕ is by using 1 and 0 instead of L and S. This is done by observing that

$$S(\phi) = \left[\operatorname{sgn}\left(\left\{\phi r + \frac{1}{2}\right\} - \left\{\phi(r+1) + \frac{1}{2}\right\}\right) + 1\right] \Big/ 2, \tag{36}$$

where $\operatorname{sgn}(x)$ is the algebraic sign of x ($+1$ or -1) for $x \neq 0$ [$\operatorname{sgn}(0)$ is defined as 0]. The previous equation can be interpreted as engineers do by looking at r as a continuous variable, say the time, and $S(\phi)$ a square wave with period ϕ sampled with frequency one. A dynamical map can be assigned to such sequence,

$$S(\phi) = \begin{cases} 1 & \text{if } \left\{\phi r + \frac{1}{2}\right\} < \phi \\ 0 & \text{otherwise} \end{cases}. \tag{37}$$

Both the symbolic sequence or the dynamical map gives what is called the Sturmian coding of a number [42], in this case ϕ. The Sturmian coding is an alternative to the continued fraction approach. It is very valuable in order to find good approximants of irrational numbers. The Sturmian coding can be easily visualized by a variant of the cut and projection. Take a square lattice, and draw a line with slope ϕ. As seen in Fig. 4(a), each intersection of this line with the verticals of the square lattice is labeled 0, and each intersection with a horizontal line is labeled 1. The labeling of the crossings is the Sturmian coding of ϕ. Notice how in Fig. 4(a) the global phason shift discussed before turns out to be very clear. By shifting the line vertically we obtain the green line that produces a global shift of the chain, which is the one that needs to be compared with the Hofstadter butterfly conductance. For irrational ϕ, the associated sequence is aperiodic and results in a Sturmian word [42].

By thinking of these sequences in terms of dynamical systems [43], we can use these trajectories on the square lattice to wrap a torus or consider a particle with constant speed that is reflected at the walls of a billiard [44]. Each 0 or 1 of the Sturmian sequence is obtained by recording the

collision with horizontal or vertical walls of a trajectory with initial slope ϕ. Figure 4(b) indicates such a procedure.

The spectrum of the map defined by Eq. (37) is made with discrete frequencies $f_{s,l}$ and amplitudes $\tilde{S}_l(\phi)$ given by

$$\tilde{S}_l(\phi) = \frac{\sin(\pi l\phi)}{\pi l}, \quad f_{sl} = s + l\phi. \tag{38}$$

In Fig. 3 it is interesting to observe how band conductances are related to band widths. This can be understood in terms of general arguments concerning the electron's wave function overlap in systems that are rational approximants to quasicrystals [45]. In fact, a dynamical map can be used to investigate the scaling exponents for critical states and relate them to each band-width scaling [45,46].

V. METHODS TO CALCULATE CHERN NUMBERS AND GLOBAL FRACTALITY

From the previous inflation/deflation rules it is possible to reverse the procedure, i.e., to obtain the Chern numbers by a simple recurrence relation. This allows one to bypass the need to solve a Diophantine equation. Such a procedure is readily obtained from observing that the Chern number for a gap r is the sum of all band conductances up to the given filling fraction [11],

$$\sigma_r = \sum_{s=1}^{r} \sigma_B(s). \tag{39}$$

We only need to find the two-letter sequence and assign to each letter its numeric counterpart. Then we sum all previous Chern numbers in the sequence for a given r. Let us show a simple example. Suppose that we want to calculate the Chern numbers for $\phi = 5/8$ without solving the Diophantine equation. We simply use the Fibonacci rule $S(\phi_j) = S(\phi_{j-2}) \oplus S(\phi_{j-1})$ to produce the sequence $S(5/8)$,

$$S(5/8) = LSLLSLSL = -3, 5, -3, -3, 5, -3, 5, -3, \tag{40}$$

where the last step requires the numerical equivalence of a letter; in this case $S \to p = 5$ and $L \to (p - q) = 5 - 8 = -3$ as $q - p$ is odd. The sequence of Chern numbers is obtained by using the recurrence relationship Eq. (39) and the initial condition $\sigma_0 = 0$,

$$\begin{aligned} \sigma_1 &= 0 - 3 = -3 \to \sigma_2 = -3 + 5 = 2 \to \sigma_3 \\ &= 2 - 3 = -1 \to \sigma_4 = -1 - 3 = -4, \end{aligned} \tag{41}$$

$$\begin{aligned} \sigma_5 &= -4 + 5 = 1 \to \sigma_6 = 1 - 3 = -2 \to \sigma_7 = -2 + 5 \\ &= 3 \to \sigma_8 = 3 - 3 = 0. \end{aligned} \tag{42}$$

A comparison with Table I reveals that the sequence is correct and valid for the Hofstadter butterfly.

When the recursion rule for a given ϕ is not known, there are two options. The first is to build the Sturmian coding of ϕ. The second option is much more efficient: Use a simple recursive test. This option works as follows. Determine the sign ζ. As always $\sigma_0 = 0$, and the next Chern number σ_1 is either $\sigma_0 - \zeta p$ or $\sigma_0 + \zeta(q - p)$. A direct substitution in the Diophantine equation gives the right choice. Once σ_1 is known, σ_2 can be calculated in a similar way. The method is iterated by using always the previous Chern number as a seed, i.e., $\sigma_{n+1} = \sigma_n - \zeta p$ or $\sigma_{n+1} = \sigma_n - \zeta(q - p)$.

Yet, there is another powerful method to find Chern numbers. This method reveals several fractal properties of the butterfly. It is based on the observation made in Sec. II that all solutions are obtained from the fundamental one, defined by the condition $\boldsymbol{F}(\phi) \cdot \boldsymbol{T}_1 = 1$. Using this fundamental solution, given by the vector $\boldsymbol{T}_1 = (\sigma_1, \tau_1)$, we define a flux $\phi' = -\tau_1/\sigma_1$, This new flux ϕ' turns out to be a Farey neighbor of ϕ. The argument is follows; for two reduced fractions $\phi = p/q$ and $\phi' = p'/q'$, the mediant is [47]

$$\frac{p''}{q''} = \frac{p + p'}{q + q'}, \tag{43}$$

and Farey neighbor fractions are required to be unimodular [47] $|p'q - pq'| = 1$. Such construction is easily visualized in two dimensions as $\boldsymbol{F}(\phi'') = (p'', q'')$ corresponds to the vectorial sum of two topological vectors,

$$\boldsymbol{F}(\phi'') = \boldsymbol{F}(\phi) + \boldsymbol{F}(\phi'). \tag{44}$$

The condition for unimodularity is

$$\boldsymbol{F}(\phi) \cdot \boldsymbol{F}^{\perp}(\phi') = \pm 1. \tag{45}$$

Thus we identify the fundamental solution with a topological vector,

$$\boldsymbol{T}_1 = \boldsymbol{F}^{\perp}(\phi') \quad \text{for} \quad \phi' = -\tau_1/\sigma_1; \tag{46}$$

in other words, we just proved that given a flux ϕ, the fundamental solution is one of its Farey neighbor's perpendicular topological vector.

Mediants occur naturally in Farey sequences, defined as fractions between 0 and 1 of a given largest denominator [47]. In this sequence, each fraction is the median of its two neighbors, and as a consequence, each flux in a Farey sequence gives its own fundamental solution by using its right neighbor fraction in the sequence. It is important to remark that the approximants of the golden ratio, given by the Fibonacci numbers, are also Farey neighbors [47].

Let us work out an example to reproduce some results of Table I. Consider the Farey sequence of order 5 built from a Farey tree [47],

$$\frac{0}{1}, \frac{1}{5}, \frac{1}{4}, \frac{1}{3}, \frac{2}{5}, \frac{1}{2}, \frac{3}{5}, \frac{2}{3}, \frac{3}{4}, \frac{4}{5}, \frac{1}{1}, \tag{47}$$

and apply it to the flux $\phi = 2/3$. Its upper Farey neighbor $\phi' = 3/4$ defines a topological vector $\boldsymbol{F}^{\perp}(3/4) = (-4, 3)$ which satisfies $\boldsymbol{F}(2/3) \cdot \boldsymbol{F}^{\perp}(3/4) = (2, 3) \cdot (-4, 3) = 1$ as expected for a Farey sequence. Thus we identify $\boldsymbol{F}^{\perp}(3/4) = \boldsymbol{T}_1 = (-4, 3)$. However, this first component $\sigma_1 = -4$ of the fundamental solution is not in the interval $[-q/2, q/2]$. We need to fold back the solution into the "Chern first Brillouin zone" by taking the modulus with $\boldsymbol{F}^{\perp}(2/3)$, as explained in Sec. II. It follows that $\boldsymbol{T}_1 = (-4, 3) + (3, -2) = (-1, 1)$ resulting in $\sigma_1 = -1$, coinciding with Table I.

This suggests the possibility of understanding the self-similarity of the topological-phase diagram by observing how phases are related at different fluxes. Indeed this is the

case. Consider the vectorial sum Eq. (44) applied to the product,

$$\boldsymbol{F}(\phi'')\cdot\boldsymbol{T}_1(\phi)=[\boldsymbol{F}(\phi)+\boldsymbol{F}(\phi')]\cdot\boldsymbol{T}_1(\phi), \tag{48}$$

where now we changed the notation to indicate that $\boldsymbol{T}_1(\phi)$ is a fundamental solution for flux ϕ, i.e., $\boldsymbol{F}(\phi)\cdot\boldsymbol{T}_1(\phi)=1$, *before doing the folding using the vector* $\boldsymbol{F}^{\perp}(\phi)$. Using this fact and that $\boldsymbol{F}(\phi')\cdot\boldsymbol{T}_1(\phi)=\boldsymbol{F}(\phi')\cdot\boldsymbol{F}_1^{\perp}(\phi')$, it follows that

$$\boldsymbol{F}(\phi'')\cdot\boldsymbol{T}_1(\phi)=1, \tag{49}$$

proving that $\boldsymbol{T}_1(\phi)$ is a fundamental solution of the mediant ϕ'' obtained from ϕ and ϕ'. It is important to remark that the solution can be folded to have Cherns between $q/2$ and $-q/2$ by using the rule $\boldsymbol{T}_1(\phi)-s\boldsymbol{F}^{\perp}(\phi'')$ for some integer s.

Consider as an example the same flux $\phi=2/3$ as before. According to the sequence (47), it has an upper Farey neighbor flux $\phi'=3/4$. The resulting mediant is $\phi''=(2+3)/(4+3)=5/7$. We have

$$\boldsymbol{F}(5/7)\cdot\boldsymbol{T}_1(2/3)=(5,7)\cdot(-4,3)=1, \tag{50}$$

as predicted. By folding back by $\boldsymbol{F}^{\perp}(5/7)=(-7,5)$ it gives the fundamental solution $(3,-1)$, i.e., the first Chern for $\phi=5/7$ is 3. It is important to remark that if we use the unfolded solution $\boldsymbol{T}_1(\phi)=(-1,1)$, instead of $(-4,3)$, we will not get the fundamental solution but a shifted one. This comes out as follows; let us consider again the product given by Eq. (48) but doing the folding before applying Eq. (49),

$$\boldsymbol{F}(\phi'')\cdot(\boldsymbol{T}_1(\phi)+s\boldsymbol{F}^{\perp}(\phi))=1+s\boldsymbol{F}(\phi')\cdot\boldsymbol{F}^{\perp}(\phi). \tag{51}$$

The product $\boldsymbol{F}(\phi')\cdot\boldsymbol{F}^{\perp}(\phi)$ although being an integer, is not zero in general, resulting in a solution different from $r=1$.

What is remarkable about Eq. (49) is that the sequence for a flux ϕ'' is contained and generated by the same solution as ϕ, as we can simply multiply Eq. (49) by r,

$$\boldsymbol{F}(\phi'')\cdot[r\boldsymbol{T}_1(\phi)]=\boldsymbol{F}(\phi'')\cdot[\boldsymbol{T}_r(\phi)]=r, \tag{52}$$

where $\boldsymbol{T}_r(\phi)$ is the solution for gap r for a ϕ which is above ϕ'' in the Farey tree. Yet the folding is dictated by ϕ'' instead of ϕ. As a matter of fact, it means that we were able to find a construction based in blocks of sequences as happens with the Fibonacci ones, but this time, for any rational flux, as the Farey tree will eventually contain any given fraction. Such construction can be seen in Fig. 3 for the fractions $1/2, 3/5, 2/3$. This helps to explain the previously numerically observed relationships between the global fractality of the butterfly and Farey neighbor sequences, as well as for its representation as Ford circles [15,16].

VI. HARPER POTENTIAL AND THE CUT AND PROJECTION METHOD

One may wonder what is behind the fact that the cut and projection method classifies the topological phases. The reason is that band gaps where topological modes reside, are open due to electron diffraction, as stationary waves are produced when the wave vector $\boldsymbol{k}$ is equal to a reciprocal lattice vector $\boldsymbol{Q}$. Thus, a vanishing group velocity $\boldsymbol{v}_g(\boldsymbol{k})$ is observed and a Van Hove singularity occurs. In fact, each gap can be labeled with two integers [48] which are related with diffraction indexes. Formally, band gaps and diffraction are related through the general formula for the density of states $\rho(\epsilon)$,

$$\rho(\epsilon)=\oint_{\boldsymbol{S}(\epsilon)}\frac{d\boldsymbol{S}}{2\pi^2|\boldsymbol{v}_g(\boldsymbol{k})|}, \tag{53}$$

where ϵ is the energy and $\boldsymbol{k}$ the wave vector. The integral is made along contours $\boldsymbol{S}(\epsilon)$ of equal energy. The group velocity is determined by the energy dispersion $\boldsymbol{v}_g(\boldsymbol{k})=\nabla_{\boldsymbol{k}}\epsilon(\boldsymbol{k})$. Whenever diffraction occurs, $|\boldsymbol{v}_g(\boldsymbol{k})|=0$. The previous formula explains the Van Hove logarithm singularities and related topological collisions at each Hofstadter butterfly band center [29].

Let us now understand how the cut and projection method is related with bands. We start our analysis by using the identity $x=\lfloor x\rfloor+\{x\}$ applied to $m\phi+\nu_y$ in the Harper potential given in Eq. (1),

$$V(m)=2\lambda\cos(2\pi\{m\phi+\nu_y\}). \tag{54}$$

Next we observe that lower band edges are obtained from $\nu_y=0$ in Eq. (1). The other limiting value $\nu_y=1/2$ gives the upper band edges [49]. As we are only interested in states at band edges, in what follows we will only consider lower band edges $\nu_y=0$ since upper band edges share the same Chern numbers as the contiguous lower band edge. In such case, using Eq. (9), we can reinterpret m as a Chern number, i.e., $m=\sigma_r$, from where the fractional part can be associated with the band index,

$$V(\sigma_r)=2\lambda\cos(2\pi\{\sigma_r\phi\})=2\lambda\cos(2\pi r/q). \tag{55}$$

Now it is clear how the argument of the cosine is associated with a wave vector $k=2\pi r/q$, having $r=0,\ldots,q-1$. Furthermore, using Eq. (55) and Eq. (27), it follows that

$$V(\sigma_r)=2\lambda\cos\left(2\pi\sqrt{1+\phi^2}\left|\boldsymbol{X}^{\perp}_{\sigma_r,\tau_r}\right|\right). \tag{56}$$

Also, as $|\boldsymbol{X}^{\perp}_{\sigma_r,\tau_r}|<1/\sqrt{1+\phi^2}$, this shows that $V(\boldsymbol{\sigma_r})$ induces an ordering of the potential according to its distances in $E^{\perp}$. Since band-level crossings do not happen [11], the ordering is preserved for all λ. Alternatively, we can say that ordering is provided by the Chern number map of Eq. (27).

Let us explain in detail the previous assertion. Following Fradkin [11], consider the limit $\lambda\to\infty$. Then $\psi^r_m\approx\delta(m-m_r)$, i.e., the wave function is a delta centered at some site m_r for band r. To find where is it localized, from Eq. (1) this will happen whenever the energy of the level is

$$E_r\approx V(m_r)=2\lambda\cos(2\pi\{m_r\phi\}). \tag{57}$$

Setting $m_r=\sigma_r$ we obtain

$$E_r\approx 2\lambda\cos(2\pi r/q)=2\lambda\cos\left(2\pi\sqrt{1+\phi^2}\left|\boldsymbol{X}^{\perp}_{\sigma_r,\tau_r}\right|\right). \tag{58}$$

The process can be summarized as follows. For a band r, the state is localized at site $m_r=\sigma_r$. Or in an alternative way, given a site $m_r=\sigma_r$, its associated band position is determined by $|\boldsymbol{X}^{\perp}_{\sigma_r,\tau_r}|$.

Notice that due to the parity of $V(m)$, the localization can also happen at $m=-\sigma_r$ for the same energy. Since for a

rational ϕ the lattice is periodic, m needs to be folded back into sites $m = 0, ..., q-1$. By performing the right folding depending whether q is odd or even, one finds that the delta functions are separated by a Chern number of sites, and results in the Chern beating phenomena discovered in Ref. [26], where edge states are a convolution of the Chern doublets with the fractal ground state [26].

Also, Aubry and Andre proved that the Harper equation is self-reciprocal [17], i.e, the Fourier coefficients of the wave function follow the same Harper equation but with λ replaced by $\lambda \to 1/\lambda$. As a result, for $\lambda \to 0$, the Fourier coefficients of the wave function are just delta localized at $k = \pm\sigma_r$ resulting in the wave function,

$$\psi_m^r \approx \frac{1}{q}\cos(2\pi\sigma_r m), \tag{59}$$

for the band r.

Here we proved that the map $r = \{\sigma_r\phi\}q$ allows one to order the energies in terms of the potential $V(\sigma_r)$, and this ordering is the same as the one for the wave-function Fourier coefficients. We can also reinterpret Eq. (55) in the original framework proposed by Hofstadter, i.e., the Bloch-Floquet theorem for the wave function in real space leads to a reordering in reciprocal space for the original wave functions [2]. The order is dictated by the perpendicular component of $\boldsymbol{X}$.

It is worthwhile mentioning that around a given flux, several topological sequences can be obtained by tilting [29] ϕ by a small amount $\delta\phi$. This is equivalent to introduce phason disorder, and as a consequence, the resulting sequences have satellites in the diffraction pattern [41]. Similar patterns are observed on graphene over a substrate [7,50].

VII. CONCLUSIONS

Using ideas from quasicrystals, we were able to find several interesting properties of the Diophantine equation which characterizes the Hofstadter butterfly as a topological-phase diagram. We showed that conductances for any given rational flux are described by symbolic sequences. Thus, conductances at different fluxes are related by inflation/deflation rules as happens for rational approximants of quasiperiodic sequences. Such rules correspond to the Sturmian sequence of the flux. They can be obtained by using a dynamical map, as trajectories in a torus, or in a square billiard, resulting in easy rules to find Chern numbers. The presented mechanism could also be valid for the square well potential which leads to the Fibonacci butterfly [22]. We also showed a higher-dimensional construction that allows one to find solutions and its self-similarity through Farey sequences, trees, and neighbors. This allows one to describe topological phases within the context of quasicrystals, and seems to be useful in order to describe complex phases in moire patterns of graphene over graphene at magical angles [4] and graphene over a substrate [7,50].

ACKNOWLEDGMENTS

I would like to thank Indu Satija for pointing out to me several properties of the Hofstadter butterfly self-similarity and Douglas Hofstadter for sharing historical perspectives on its discovery. Both events happened during a sabbatical leave at George Mason University, Fairfax, Virginia, USA. The author wishes to thank George Mason Department of Physics for hospitality there. This work has been supported by DGAPA-UNAM Project No. IN102717.

[1] D. J. Thouless, M. Kohmoto, M. P. Nightingale, and M. den Nijs, Phys. Rev. Lett. **49**, 405 (1982).
[2] D. R. Hofstadter, Phys. Rev. B **14**, 2239 (1976).
[3] C. R. Dean, L. Wang, P. Maher, C. Forsythe, F. Ghahari, Y. Gao, J. Katoch, M. Ishigami, P. Moon, M. Koshino, T. Taniguchi, K. Watanabe, K. L. Shepard, J. Hone, and P. Kim, Nature (London) **497**, 598 (2013).
[4] G. Tarnopolsky, A. J. Kruchkov, and A. Vishwanath, Phys. Rev. Lett. **122**, 106405 (2019).
[5] M. Z. Hasan and C. L. Kane, Rev. Mod. Phys. **82**, 3045 (2010).
[6] C. L. Kane and E. J. Mele, Phys. Rev. Lett. **95**, 146802 (2005).
[7] P. Roman-Taboada and G. G. Naumis, Phys. Rev. B **90**, 195435 (2014).
[8] G. G. Naumis, S. Barraza-López, M. Oliva-Leyva, and H. Terrones, Rep. Prog. Phys. **80**, 096501 (2017).
[9] I. N. Karnaukhov, Phys. Lett. A **383**, 2114 (2019).
[10] R. A. El-Nabulsi, J. Phys. Chem. Solids **127**, 224 (2019).
[11] E. Fradkin, *Field Theories of Condensed Matter Physics*, 2nd ed. (Cambridge University Press, Cambridge, 2013).
[12] H.-L. Yu, Z.-Y. Zhai, and X.-T. Bian, Chin. Phys. Lett. **33**, 117305 (2016).
[13] H. L. Yu and Z. Y. Zhai, Modern Phys. Lett. B **32**, 1850158 (2018).
[14] I. N. Karnaukhov, J. Phys. Commun. **1**, 051001 (2017).
[15] I. I. Satija, *Butterfly in the Quantum World*, 2053–2571 (Morgan & Claypool Publishers, San Rafael, 2016).
[16] I. I. Satija, Eur. Phys. J. Spec. Top. **225**, 2533 (2016).
[17] S. Aubry and G. André, Ann. Israel Phys. Soc **3**, 18 (1980).
[18] P. G. Harper, Proc. Phys. Soc. A **68**, 879 (1955).
[19] I. Dana, Y. Avron, and J. Zak, J. Phys. C: Solid State Phys. **18**, L679 (1985).
[20] C. Janot, *Quasicrystals: A Primer*, *Monographs on the Physics and Chemistry of Materials* (Oxford University Press, Oxford, 2012).
[21] W. Steurer and S. Deloudi, in *Crystallography of Quasicrystals*, Vol. 126 (Springer-Verlag, Berlin/Heidelberg, 2009), pp. XIV, 384.
[22] G. Naumis and F. López-Rodríguez, Physica B: Condens. Matter **403**, 1755 (2008).
[23] Y. E. Kraus, Y. Lahini, Z. Ringel, M. Verbin, and O. Zilberberg, Phys. Rev. Lett. **109**, 106402 (2012).
[24] Y. E. Kraus and O. Zilberberg, Phys. Rev. Lett. **109**, 116404 (2012).
[25] G. Amit and I. Dana, Phys. Rev. B **97**, 075137 (2018).
[26] I. I. Satija and G. G. Naumis, Phys. Rev. B **88**, 054204 (2013).
[27] D. J. Apigo, W. Cheng, K. F. Dobiszewski, E. Prodan, and C. Prodan, Phys. Rev. Lett. **122**, 095501 (2019).
[28] Y. Barlas and E. Prodan, Phys. Rev. B **98**, 094310 (2018).

[29] G. G. Naumis, Phys. Lett. A **380**, 1772 (2016).
[30] F. Flicker and J. van Wezel, Europhys. Lett. **111**, 37008 (2015).
[31] D. Levine and P. J. Steinhardt, Phys. Rev. B **34**, 596 (1986).
[32] G. G. Naumis, Phys. Rev. B **71**, 144204 (2005).
[33] M. Baake and U. Grimm, *Aperiodic Order*, *Encyclopedia of Mathematics and Its Applications*, Vol. 2 (Cambridge University Press, Cambridge, 2017).
[34] S. Acheche, L.-F. Arsenault, and A.-M. S. Tremblay, Phys. Rev. B **96**, 235135 (2017).
[35] I. E. Powell and S. Chakravarty, Phys. Rev. B **100**, 075150 (2019).
[36] Y. Hatsugai and M. Kohmoto, Phys. Rev. B **42**, 8282 (1990).
[37] F. H. Claro and G. H. Wannier, Phys. Rev. B **19**, 6068 (1979).
[38] G. Naumis and J. Aragón, Z. Kristallogr. - Crystalline Materials **218**, 397 (2003).
[39] J. L. Aragón, G. G. Naumis, and M. Torres, Acta Crystallographica Section A **58**, 352 (2002).
[40] E. Maciá Barber, Crystals **7**, 64 (2017).
[41] G. G. Naumis, C. Wang, M. F. Thorpe, and R. A. Barrio, Phys. Rev. B **59**, 14302 (1999).
[42] N. P. Fogg, *Substitutions in Dynamics, Arithmetics and Combinatorics* (Springer Science & Business Media, Berlin, 2002).
[43] M. Baake, D. Lenz, and R. Moody, Ergodic Theory Dynamical Systems **27**, 341 (2007).
[44] N. Bedaride, Theor. Comput. Sci. **385**, 214 (2007).
[45] G. G. Naumis, Phys. Rev. B **59**, 11315 (1999).
[46] G. G. Naumis, J. Phys.: Condens. Matter **15**, 5969 (2003).
[47] M. Schroeder, *Fractals, Chaos, Power Laws: Minutes from an Infinite Paradise* (Courier Corporation, North Chelmsford, 2009).
[48] J. Kellendonk, Rev. Math. Phys. **07**, 1133 (1995).
[49] D. J. Thouless, Phys. Rev. B **28**, 4272 (1983).
[50] P. Roman-Taboada and G. G. Naumis, Phys. Rev. B **92**, 035406 (2015).